DOI 10.4430/bgo00373

The full-field apparent resistivity of CSAMT defined by the magnetic field *y*-component and an application to a geological survey in the Xiong'an New Area, China

J. Wang[1,2], M. Wang[1,3], W. Liu[2] and P. Lin[2]

[1] *School of Geophysics and Information Technology, China University of Geosciences, Beijing, China*

[2] *Institute of Geophysical and Geochemical Exploration, Chinese Academy of Geological Sciences, Langfang, China*

[3] *China Aero Geophysics Survey & Remote Sensing Center for Land and Resources, Beijing, China*

(Received: 12 December 2020; accepted: 14 August 2021; published online: 14 February 2022)

ABSTRACT Controlled source audio magnetotelluric (CSAMT) has good depth penetration and high data quality. However, the Cagniard apparent resistivity calculated in the near-field zone and transition zone is distorted, and collecting electric field components in some specific landscapes requires a high cost, such as desert, permafrost, and water areas. The magnetic field *y*-component (H_y) is not restricted by bad electrode grounding conditions, and the signal level is greater than that of the magnetic field *z*-component (H_z), which can be used to obtain the ground resistivity. A simple algorithm was used to calculate the apparent resistivity defined by H_y, and the response characteristics and measurement range were analysed by model calculation. The results show that the H_y full-field apparent resistivity has no obvious distortion. This method is applied to geological surveys in the Xiong'an New Area, China. The results indicate that the detection depth of the H_y full-field apparent resistivity is better than that of electric field *x*-component (E_x), and the signal-to-noise ratio is better than that of H_z. Moreover, the 1D and 2D inversion results are in good agreement with the known geological conditions. This method can extend the observational conditions and range of CSAMT.

Key words: CSAMT, apparent resistivity, modelling, inversion, mapping.

1. Introduction

Controlled source audio magnetotelluric (CSAMT) is a frequency domain electromagnetic method developed from the magnetotelluric (MT) method (Goldstein and Strangway, 1975). By using an artificial source, the CSAMT overcomes problems associated with the weak natural source used in the MT method, which has been widely used for mineral, engineering, and hydrology surveys (Wang *et al*., 2016; Lei *et al*., 2017). In conventional onshore CSAMT work, a set of orthogonal electromagnetic (EM) field components are measured in the far-field zone, and the Cagniard apparent resistivity can be calculated (Zonge and Hughes, 1991). However, under a nonplane-wave effect, the Cagniard apparent resistivity calculated in the near-field zone and

© 2022 - OGS

transition zone will be distorted, and it will not be able to truly reflect the underground resistivity (Shlykov and Saraev, 2014; Lei *et al*., 2016). Although the Cagniard apparent resistivity data from the near-field zone, transition zone, and far-field zone can be used in the full CSAMT inversion (Routh and Oldenburg, 1999; Asten *et al.*, 2005), the distorted apparent resistivity parameters cannot provide an ideal initial inversion model, and the results are often unsatisfactory due to the non-uniqueness of inversion (Bai and Meju, 2003).

There are two major categories of approaches used to eliminate the nonplane-wave effect. The first approach corrects the Cagniard apparent resistivity directly (Bartel and Jacobson, 1987; Luan *et al*., 2018). However, this compromises the resistivity information that can be obtained from the transition zone data (Maurer, 1988; Boerner *et al*., 1993); additionally, it is difficult to evaluate the reliability of the correction results under complex electrical structure conditions. The second approach converts the EM field to a new apparent resistivity, which can better approximate the true resistivity of the earth and suppress the false extreme phenomenon (Wilt and Stark, 1982; Spies and Eggers, 1986; Umesh, 1995; Asten *et al.*, 2005). With the improvement in the calculation ability, the full-field apparent resistivity can be calculated directly from the implicit equation of the EM field, overcoming the limitation of the far-field zone observation (Sternberg, 1979; Tang and He, 2005; He, 2010). In addition, the ground resistivity could be obtained by observing single electric or magnetic components, which changed the traditional observation mode of CSAMT (Xue, 2018).

Due to the high resistivity sensitivity and low data acquisition cost, the electric field *x*-component (E_x) is currently the most studied component (Li, 2017; Liu *et al*., 2018; Hou *et al*., 2019). In contrast to the electric field component, the magnetic field is not susceptible to static effects and is not limited by the ground contact conditions, which can play an important role in areas with bad electrode grounding conditions, such as the Gobi Desert and permafrost and water areas. The full-field apparent resistivity defined by the vertical magnetic field (H_z) has been used for the exploration on the ice (Chen and Xue, 2015). In the far-field zone, however, the amplitude of H_z is inversely proportional to the fourth power of the source-sounding separation *r*. When *r* is large, it is difficult to ensure a high signal-to-noise ratio (SNR), which limits the measurement range.

Theoretically, the amplitude of H_y is inversely proportional to the third power of *r* in the far-field zone, which is obviously larger than that of H_z. At present, conversion of the measured H_y data into the full-field apparent resistivity parameters has not been a popular method. The Bessel function needs to be calculated to obtain H_y for a homogeneous earth, which increases the computational complexity; additionally, some special phenomena may occur in the calculation of apparent resistivity, such as there being no solution or double solutions (Umesh, 1995). In this paper, we first analysed the response characteristics of H_y. Next, the algorithm for calculating the H_y full-field apparent resistivity was introduced. Then, we compared the response characteristics of different apparent resistivities for a homogeneous earth and layered models and analysed the measurement range of H_y. Finally, a data set example from the Xiong'an New Area was used to demonstrate the practical efficacy of the H_y full-field apparent resistivity.

2. Theory

2.1. EM field of CSAMT

The coordinate systems are shown in Fig. 1. For a horizontal electrical dipole source at the surface of a homogeneous earth with conductivity σ (S/m), the surface E_x, H_y, and H_z can be

expressed as follows (Tang and He, 2005):

$$E_x = \frac{IdL}{2\pi\sigma r^3}\left[3\cos^2\varphi - 2 + e^{\mathrm{i}kr}(1-\mathrm{i}kr)\right] \quad (1)$$

$$H_y = -\frac{IdL}{4\pi r^2}\{\sin^2\varphi[6I_1K_1 + \mathrm{i}kr(I_1K_0 - I_0K_1)] - \cos^2\varphi\, I_1K_1\} \quad (2)$$

$$H_z = -\frac{IdL}{2\pi\sigma r^4\mu\omega}\sin\varphi\left[3 - e^{\mathrm{i}kr}(3 - 3\mathrm{i}kr - k^2r^2)\right] \quad (3)$$

where *dL* (in m) is the length of the dipole along the direction of the x-axis; *I* (in A) is the current, where the frequency is ω (rad/s); *r* (in m) is the distance between source and sounding; φ (in degree) is the angle between *r* and x-axis; μ (in H/m) is the magnetic permeability; $k = \sqrt{\mathrm{i}\omega\mu\sigma}$ is the propagation constant; i is an imaginary number; and I_m and K_m are first- and second-kind modified Bessel functions of the *m*-th order, respectively. In field work, a finite source is usually used to increase the signal strength, which can be simulated by the sum of a series of dipoles.

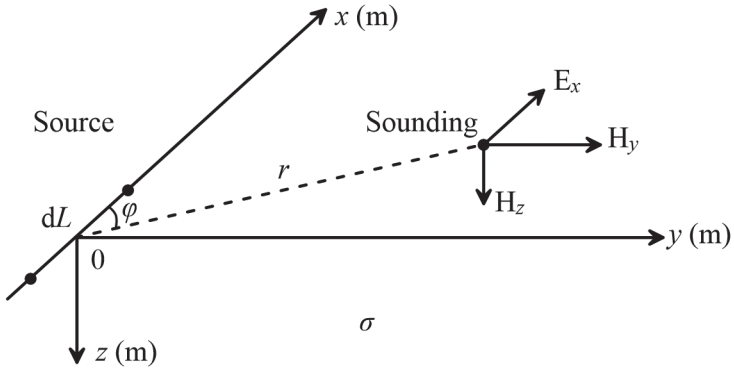

Fig. 1 - Sketch of coordinate system and EM components in CSAMT.

For the convenience, we use $|kr| >> 1$ and $|kr| \ll 1$ to distinguish the far-field zone and near-field zone. The limits of Eqs. 1 to 3 for $|kr| >> 1$ and $|kr| \ll 1$ are listed in Table 1 (Zonge and Hughes, 1991; Tang and He, 2005).

Table 1 - The limits of the EM field in the far-field zone and near-field zone.

Component	$\|kr\| >> 1$	$\|kr\| \ll 1$
E_x	$E_x \approx \frac{IdL}{2\pi r^3\sigma}(3\cos^2\varphi - 2)$	$E_x \approx \frac{IdL}{2\pi r^3\sigma}(3\cos^2\varphi - 1)$
H_y	$H_y \approx \frac{IdL}{2\pi r^3\sqrt{\omega\mu\sigma}}e^{\mathrm{i}\frac{\pi}{4}}(3\cos^2\varphi - 2)\mathrm{i}$	$H_y \approx \frac{IdL}{4\pi r^2}e^{i\frac{\pi}{4}}(1 - 2\cos^2\varphi)$
H_z	$H_z \approx -\frac{3IdL}{2\pi r^4\omega\mu\sigma}\sin\varphi$	$H_z \approx -\frac{IdL}{4\pi r^2}\sin\varphi$

Table 1 shows that the EM field of the far-field zone is related to the frequency and conductivity, which means that these components contain the frequency sounding information. In the near-field zone, the EM field is independent of frequency, and the magnetic field has nothing to do with conductivity. In the transition zone, these components are complex functions related to the conductivity and frequency, which contain geoelectric information.

2.2. Full-field apparent resistivity

The full-field apparent resistivity can be derived from Eqs. 1 to 3:

$$\rho_s^{E_x} = \frac{2\pi r^3}{I\mathrm{d}L}\left[\frac{E_x}{3\cos^2\varphi - 2 + e^{\mathrm{i}kr}(1-\mathrm{i}kr)}\right] \tag{4}$$

$$\rho_s^{H_y} = \frac{16\pi^2 r^6}{I^2\mathrm{d}L^2}\mu\omega\left[\frac{H_y}{\{\sin^2\varphi[6I_1K_1 + \mathrm{i}kr(I_1K_0 - I_0K_1)] - 2\cos^2\varphi\, I_1K_1\}kr}\right]^2 \tag{5}$$

$$\rho_s^{H_z} = \frac{2\pi r^4}{I\mathrm{d}L\sin\varphi}\mu\omega\left[\frac{H_z}{3 - e^{\mathrm{i}kr}(3 - 3\mathrm{i}kr - k^2r^2)}\right] \quad (\varphi \neq 0^\circ) \tag{6}$$

For a homogeneous earth, apparent resistivity is equal to the true resistivity value. Otherwise, apparent resistivity is the equivalent resistivity when the medium is regarded as a homogeneous earth. The limits of Eqs. 4 to 6 for $|kr| \gg 1$ and $|kr| \ll 1$ are listed in Table 2 (Tang and He, 2005).

Table 2 - The limits of the full-field apparent resistivity in the far-field zone and near-field zone.

Component	$\|kr\| >> 1$	$\|kr\| \ll 1$
$\rho_s^{E_x}$	$\rho^{E_x} \approx \frac{2\pi r^3}{I\mathrm{d}L}\left(\frac{E_x}{3\cos^2\varphi - 2}\right)$	$\rho^{E_x} \approx \frac{2\pi r^3}{I\mathrm{d}L}\left(\frac{E_x}{3\cos^2\varphi - 1}\right)$
	ρ^{H_y}	
$\rho_s^{H_y}$	$\approx \frac{4\pi^2 r^6}{I^2\mathrm{d}L^2}\mu\omega\left(\frac{H_y}{3\cos^2\varphi - 2}\right)^2$	$\rho^{H_y} \approx \frac{16\pi^2 r^4}{I^2\mathrm{d}L^2\sigma}\left(\frac{H_y}{1 - 2\cos^2\varphi}\right)^2$
$\rho_s^{H_y}$	$\rho^{H_z} \approx \frac{2\pi r^4}{3I\mathrm{d}L\sin\varphi}\mu\omega H_z$	$\rho^{H_z} \approx \frac{4\pi r^2}{I\mathrm{d}L\,\sigma\sin\varphi}H_z$

Table 2 shows that the full-field apparent resistivity of the far-field zone is equal to the far-field apparent resistivity. In the near-field zone, the full-field apparent resistivity defined by the magnetic field converges to a constant, which is related to the resistivity of the maximum transmission depth of the primary field. For a homogeneous earth, this constant is equal to the true resistivity value. Otherwise, the constant is related to the geoelectric parameters and device parameters. Therefore, the full-field apparent resistivity is closer to the real model, which can provide an initial inversion model without obvious distortion.

3. Response characteristics of H_y

Using Eqs. 2 and 3, we calculated the H_y and H_z for a homogeneous earth. Fig. 2 shows that the high-signal-level zones of H_y are in good agreement with the measurement zones for scalar CSAMT configuration given by Zonge and Hughes (1991). Hence, broadside and collinear H_y data can be used to obtain ground resistivity. Table 1 shows that the amplitude of H_z is inversely proportional to the fourth power of r in the far-field zone, whereas that of H_y is inversely proportional to the third power of r. The numerical simulation results show that H_y is 1 to 3 orders of magnitude higher than H_z at high frequencies. Under high noise levels, the SNR of H_y is better than that of H_z. Moreover, the earth resistivity is linear with H_z and varies as the square root of H_y, which indicates that H_y is less sensitive to resistivity.

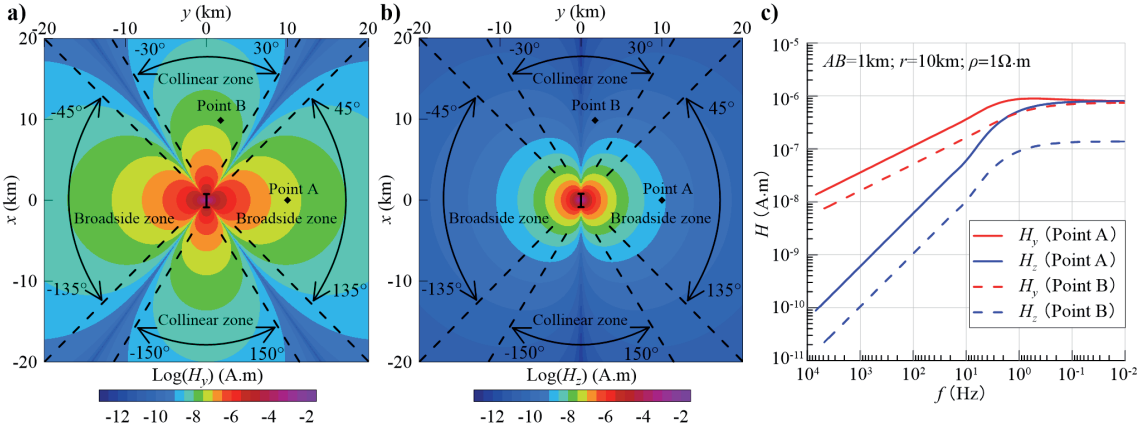

Fig. 2 - The amplitudes of H_y (a) and H_z (b) for a homogeneous half-space at a frequency of 500 Hz and the normalised magnetic field responses at two receiver points (c).

Fig. 3 shows the frequency characteristic curves of H_y with different resistivities. In the far-field zone, H_y increases rapidly with decreasing frequency, and the H_y values in the broadside zones are twice as high as those in the collinear zones. With decreasing resistivity, the frequency range of the far-field zone shifts to lower frequencies. Therefore, H_y is more suitable for sounding in low-resistivity areas.

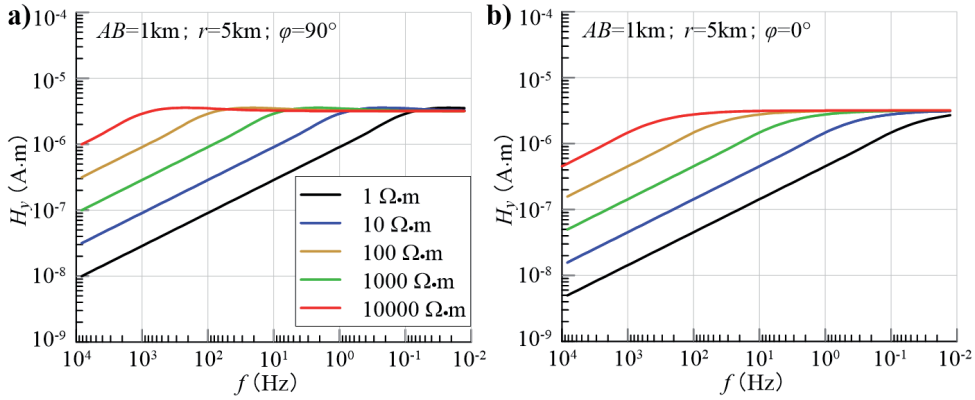

Fig. 3 - The frequency characteristic curves of H_y with different resistivities: a) "broadside" H_y curves; b) "collinear" H_y curves.

The shape of the frequency characteristic curve leads to some specific phenomena in the calculation of the apparent resistivity. First, there are obvious differences between Figs. 3a and 3b in the transition zone. The collinear H_y, shown in Fig. 3b, has a simple one-to-one correspondence with resistivity similar to that of E_x and H_z. In Fig. 3a, however, the broadside H_y is not a monotonic function of resistivity, which induces the double-solution phenomenon using collinear H_y to calculate the apparent resistivity. Second, because of the complex geoelectric structure or random noise, the observed H_y may exceed the maximum value calculated for a homogeneous earth. That is, the apparent resistivity appears to be a no-solution phenomenon. Moreover, the sensitivity of H_y to the resistivity decreases with decreasing frequency. In field work, a small EM noise in the observation data may lead to large errors in the full-field apparent resistivity, and the reliability of results will be reduced.

4. Calculation of the full-field apparent resistivity defined by H_y

In Eq. 5, the resistivity and the EM fields are complex implicit functions, which can be solved by the numerical iteration algorithm with successive approximations (Sternberg, 1979). To address the double-solution phenomenon, one method is to obtain the double solution by piecewise fitting and then choose the more reasonable solution. Based on the assumption that the apparent resistivity curve changes smoothly and the turning amplitude is as small as possible, an iteration scheme with minimum curvature was used to smooth the transition section of the double solutions in time-domain transient electromagnetic method (Zhang *et al*., 2015). This algorithm can also be used to interpolate the 'null' points when there is no solution.

For the collinear H_y, we calculate the full-field apparent resistivity from the high-frequency end to the low-frequency end, and the following steps are used:

1 - judge the existence of solutions. It is assumed that the resistivity of the underground medium is in the range of 10^{-1} to 10^5 Ω·m (Keller, 1988). For the given frequency and geometric parameters, the maximum H_y value can be calculated using Eq. 2. If the measured H_y is larger than the theoretical maximum H_y, there is no solution, and the next frequency point is determined;
2 - set the initial value. For the first frequency point, the far-field apparent resistivity can be used; for others, the result of the previous frequency can be used, which can reduce the number of iterations;
3 - obtain the solution. By iteratively modifying the resistivity, when the error between the calculated H_y and the measured H_y is less than the threshold, the optimal solution is obtained. Using the above steps, the solutions of all frequencies are calculated;
4 - interpolate. Finally, the solutions at all frequencies are checked, and the no-solution points can be interpolated using an iteration scheme with minimum curvature.

For the broadside H_y, step 3 needs to be replaced by the following steps:

5 - obtain all solutions. If the H_y calculated in step 1 increases or decreases monotonically (section I and III in Fig. 4a), a unique solution can be obtained by iteratively fitting the measured H_y. If the calculated H_y is not monotonic (section II), then it is judged whether the observed H_y is located in the monotonic section or not. If the observed H_y is located in the monotonic section (section II-b), a unique solution can also be obtained; otherwise, two solutions can be obtained (Fig. 4b);
6 - select the reasonable solutions. In the double logarithmic coordinate system, if the relative deviation of the two solutions is large (e.g. > 80%), the solution, which is closer to that of the previous frequency, is chosen. Other cases are considered as having no solution (Fig. 4c).

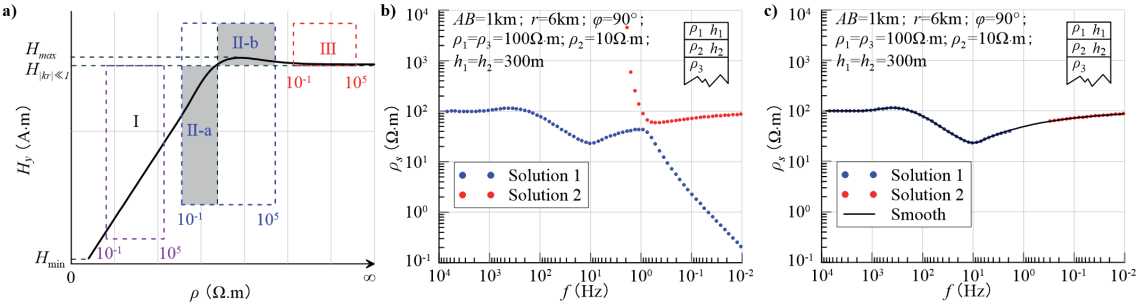

Fig. 4 - The process of calculating the full-field apparent resistivity with the broadside H_y: a) schematic diagram of how to judge the monotonic section of the calculated H_y; b) double-solution phenomenon; c) selection the reasonable solutions and interpolation.

This approach was applied to the 'H-curve' model. Fig. 4b shows that the double solutions begin to appear near 2 Hz, and the full-field apparent resistivity curve is smooth. In the transition zone, the full-field apparent resistivity gradually transitions from the far-field apparent resistivity to a constant related to the geoelectric parameters. Although H_y is independent of the resistivity in the near-field zone, we can obtain a stable value using our algorithm. This is due to the proper calculation order and the initial value of the iteration.

5. Modelling

5.1. Homogeneous Earth

Fig. 5 illustrates the comparison of the H_y full-field apparent resistivity, Cagniard apparent resistivity and H_y far-field apparent resistivity. After entering the transition zone and near-field zone, the curves of the far-field apparent resistivity and the Cagniard apparent resistivity decrease and increase, respectively, in an asymptotic line at an angle of 45°. The values of the H_y full-field apparent resistivity are 100 Ω·m in the whole frequency band, which objectively reflects the geoelectric model.

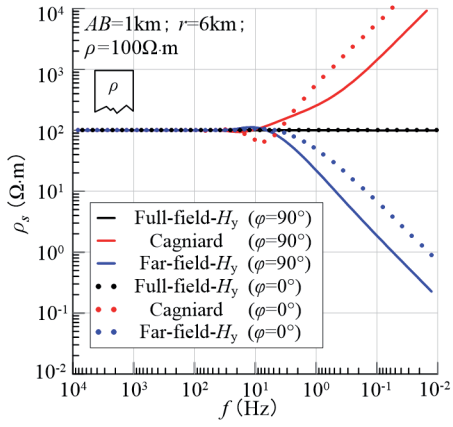

Fig. 5 - Calculation results of the homogeneous half-space model.

5.2. Layered model

Fig. 6 shows the apparent resistivity curves of a two-layered model for various resistivity contrasts, where $\lambda = 2\pi\sqrt{2\rho_1/\mu\omega}$. Neither the high- nor low-resistance basement can be truly reflected by the Cagniard apparent resistivity curves. The full-field apparent resistivity curves respond well to basements with different resistivities. In Fig. 6, the tail branch asymptotes of the H_y full-field apparent resistivity curves appear at lower frequencies than that of E_x, which can better reflect the real resistivity of the deep layer. The H_y full-field apparent resistivity curves are similar to the Cagniard apparent resistivity curves of MT method.

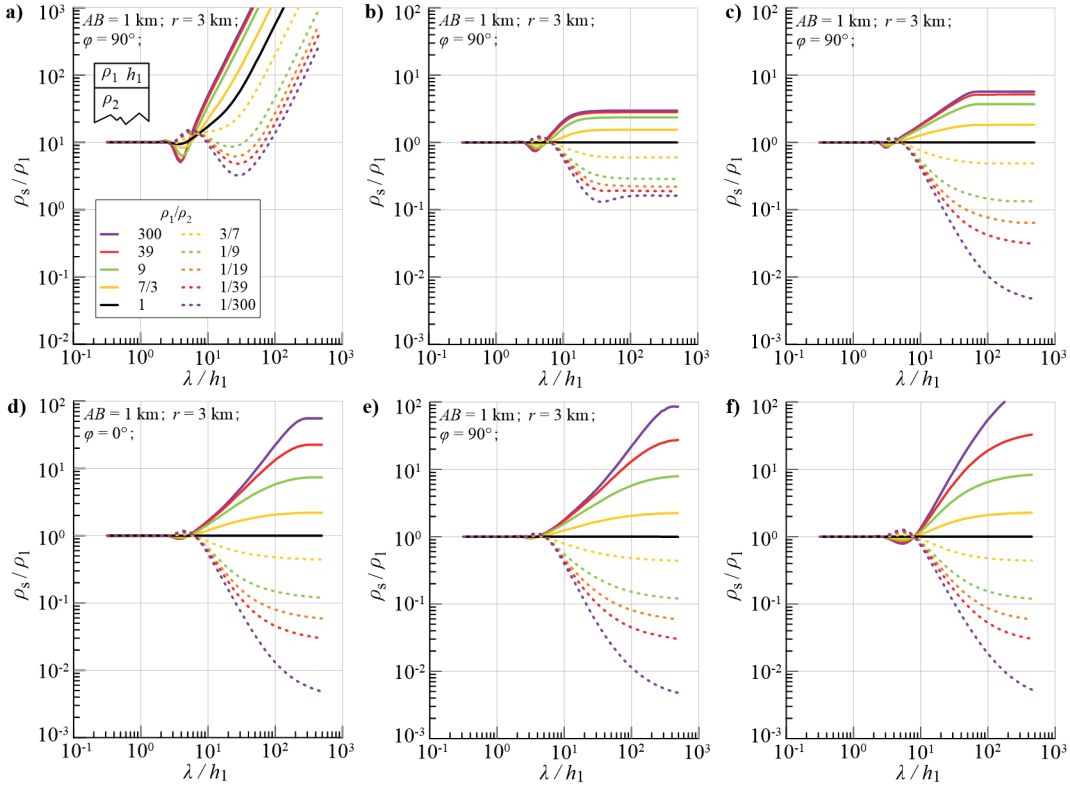

Fig. 6 - Calculation results of the two-layered model (after He, 2010): a) Cagniard apparent resistivity of CSAMT; b) E_x full-field apparent resistivity; c) H_z full-field apparent resistivity; d) H_y full-field apparent resistivity in the collinear zone; e) H_y full-field apparent resistivity in the broadside zone; f) Cagniard apparent resistivity of MT method.

In Fig. 7, another 'D-curve' two-layered model is established to analyse the ability of the apparent resistivity to penetrate a thick screening layer. In Fig. 7a, the full-field apparent resistivity curves defined by the magnetic field are effective in reflecting the low-resistivity basement under the overburden, and these curves are similar to that of the Cagniard apparent resistivity of MT method. However, the E_x full-field apparent resistivity has only a very slight response. In Fig. 7b, the influence of the separation r is analysed. Although the values of the tail branch gradually approach the true resistivity value with increasing r, the H_y full-field apparent resistivity is less affected by r. A good penetration depth can be achieved with a small r, which allows us to increase the signal level by reducing r.

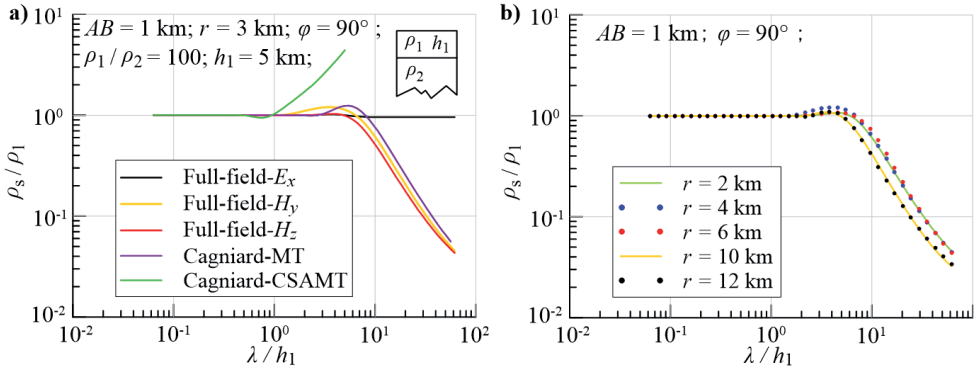

Fig. 7 - Calculation results of the 'D-curve' two-layered model with a thick high-resistance overburden: a) comparison of different apparent resistivity curves; b) the H_y full-field apparent resistivity curves with different r values.

In Fig. 8, the 'K-curve' three-layered model is simulated. The tail branches of the H_y and H_z full-field apparent resistivity curves approach the true resistivity value of the bottom layer, while that of E_x produces a large value. In Fig. 8b, the influence of noise on the full-field apparent resistivity was analysed. Gaussian noise with a standard deviation of 5% was added to H_y. The errors of the full-field apparent resistivity calculated by H_y increase rapidly at low frequencies. Therefore, to improve the SNR, it is necessary to adopt a small r that satisfies the detection depth.

Angle φ has a great influence on the E_x full-field apparent resistivity, and acceptable angles φ are -20° to 20° and 60° to 120° (Li, 2017). The 'K-curve' model is also used to analyse the influence of φ on the H_y full-field apparent resistivity. In the measurement zones given by Zonge and Hughes (1991), the H_y full-field apparent resistivity has no obvious distortion, as shown in Fig. 9. The H_y has a larger measurement angle range than E_x. Using the H_y full-field apparent resistivity, a large area can be surveyed with few transmitters, which improves the logistic efficiency and reduces the source effects.

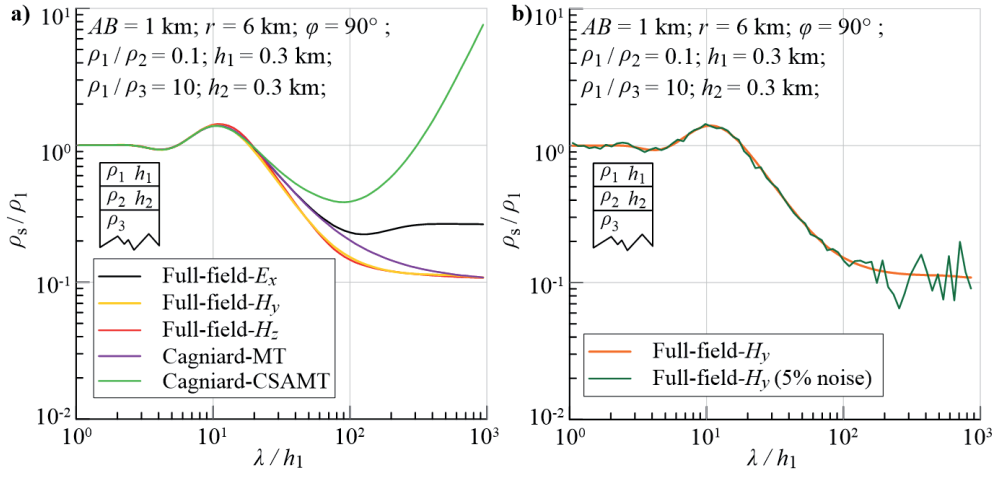

Fig. 8 - Calculation results of the 'K-curve' three-layer model: a) comparison of different apparent resistivity curves; b) full-field apparent resistivity when the noise level is 5%.

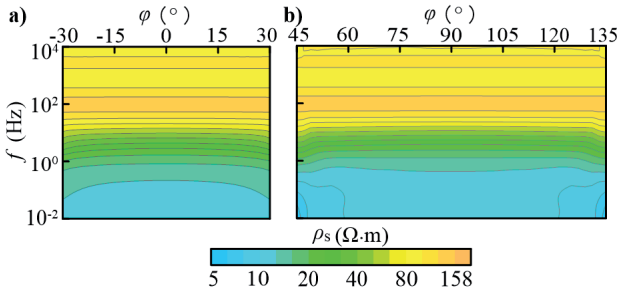

Fig. 9 - Variation in the H_y full-field apparent resistivity with angle φ.

6. Application example

6.1. Arrangement

The Xiong'an New Area is a being constructed new area in China that can support 2-2.5 million people. A comprehensive geophysical survey can provide important geological support for the overall program and construction of the new area. There are 143 large and small shallow lakes in the area, and the average water depth is 3.6 m. Within the 50 m to 2 km depth range, the CSAMT produces high-quality data quickly, especially in an area typified by high cultural (arisen from man-made metallic structures and radio station) noise. However, it is difficult to collect electric field signals in a water area, so the magnetic field can play an important role.

The test area is widely covered by Quaternary sediments (Fig. 10). Drill hole D18 is 1.5 km north of point 299. The drilling revealed that the floor depths of the Quaternary, Neogene and Paleogene ages are 430, 1341.8, and 2119 m, respectively (Wang *et al.*, 2018). The underlying stratum is dolomite of the Mesoproterozoic Jixian system (1400-1000 Myr). Field work was carried out in January, when the large area of water was frozen. The original data were provided by the CLEM-VI system (Wang *et al.*, 2017, 2019). To improve the SNR of the EM signal, the transmitter current reached 45 A (1 Hz). To compare the full-field apparent resistivity as defined by E_x,

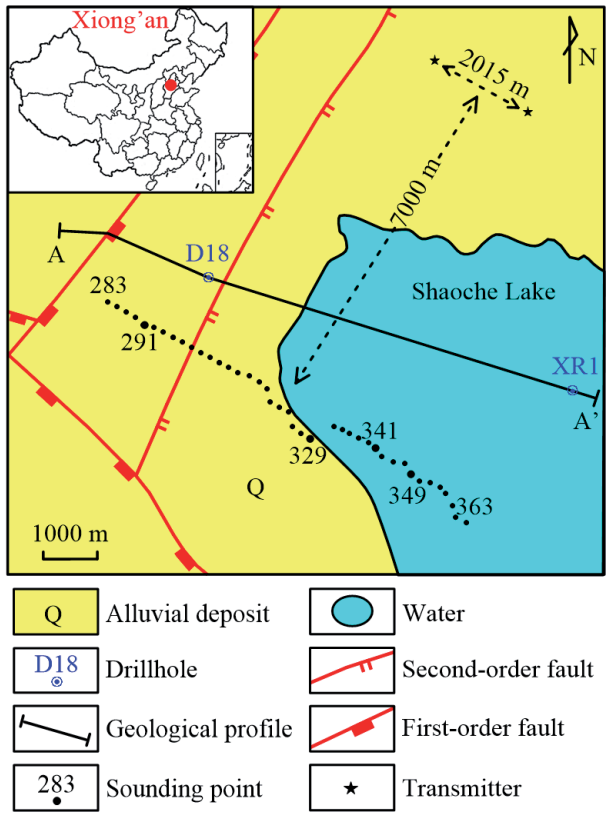

Fig. 10 - Layout of CSAMT in the study area (after Wang *et al.*, 2018).

H_y, and H_z, broadside measurements were chosen. Points 283 to 329 are on land, and points 333 to 363 are in the water area. The E_x and H_y data were obtained on land, and the H_y and H_z data were obtained in the water area. The E_x is sensed by an electric dipole whose length is 200 m.

6.2. Results

Compared with the apparent resistivity curves defined by H_z, those of E_x and H_y are smoother and more continuous (Fig. 11). At point 341, the data quality of H_z is the highest among all measurement points. Similar conclusions can be drawn from the pseudo-section in Fig. 11. Although the three subfigures are similar in their overall shapes, they have some differences. The responses of H_y and H_z to the high-resistance basement are more obvious than E_x.

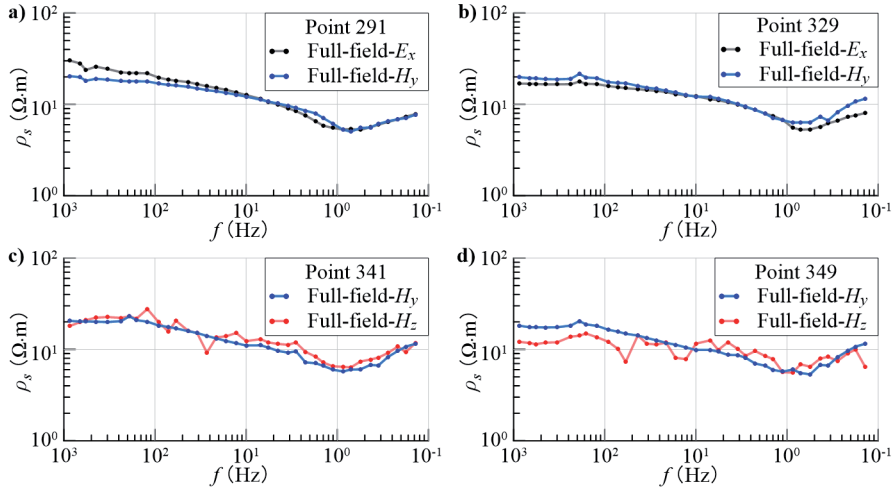

Fig. 11 - Curves of the full-field apparent resistivity observed at point 291 (a), point 329 (b), point 341 (c) and point 349 (d).

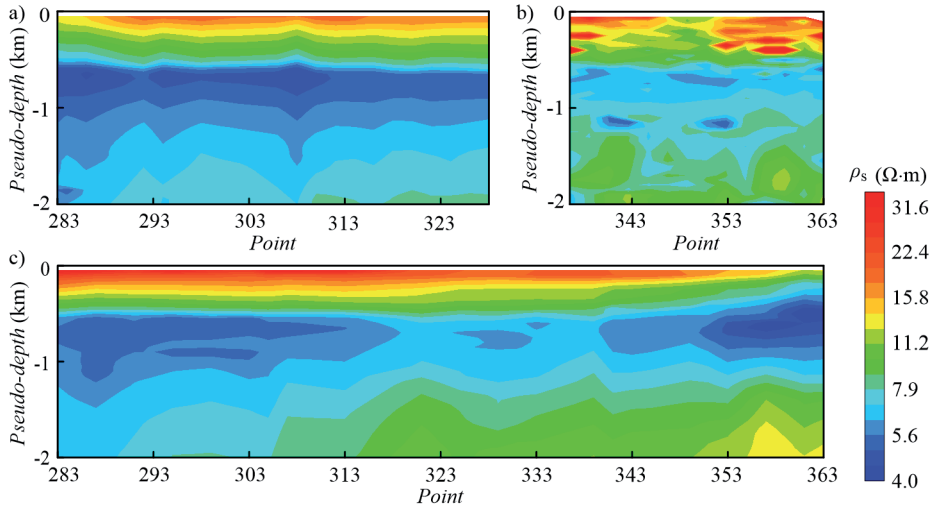

Fig. 12 - The E_x(a) H_z(b), and H_y (c) full-field apparent resistivity pseudo-sections.

Finally, smooth inversions of the H_y full-field apparent resistivity were carried out. In 1D inversion, the variable step size difference accumulation algorithm was used to calculate the sensitivity matrix (Wang *et al.*, 2015). As the H_y full-field apparent resistivity curves are similar to the Cagniard apparent resistivity curves of MT, 2D inversion algorithm of MT was adopted to generate the resistivity profile. Fig. 13 shows that the inversion results are in good agreement with the known geological setting. Based on the geological profile, the resistivity profile can be divided longitudinally into three sections. The high resistivity of the shallow level corresponds to the alluvial deposits of the Quaternary. In the middle part, the middle- and low-resistivity zones are attributed to mudstone of the Neogene and Paleogene. The deep high-resistivity zone indicates the dolomite in the Wumishan Formation of the Jixian System. The depths of the Quaternary and Jixian Systems are deep in the west and shallow in the east, which is clearly reflected in the inversion results.

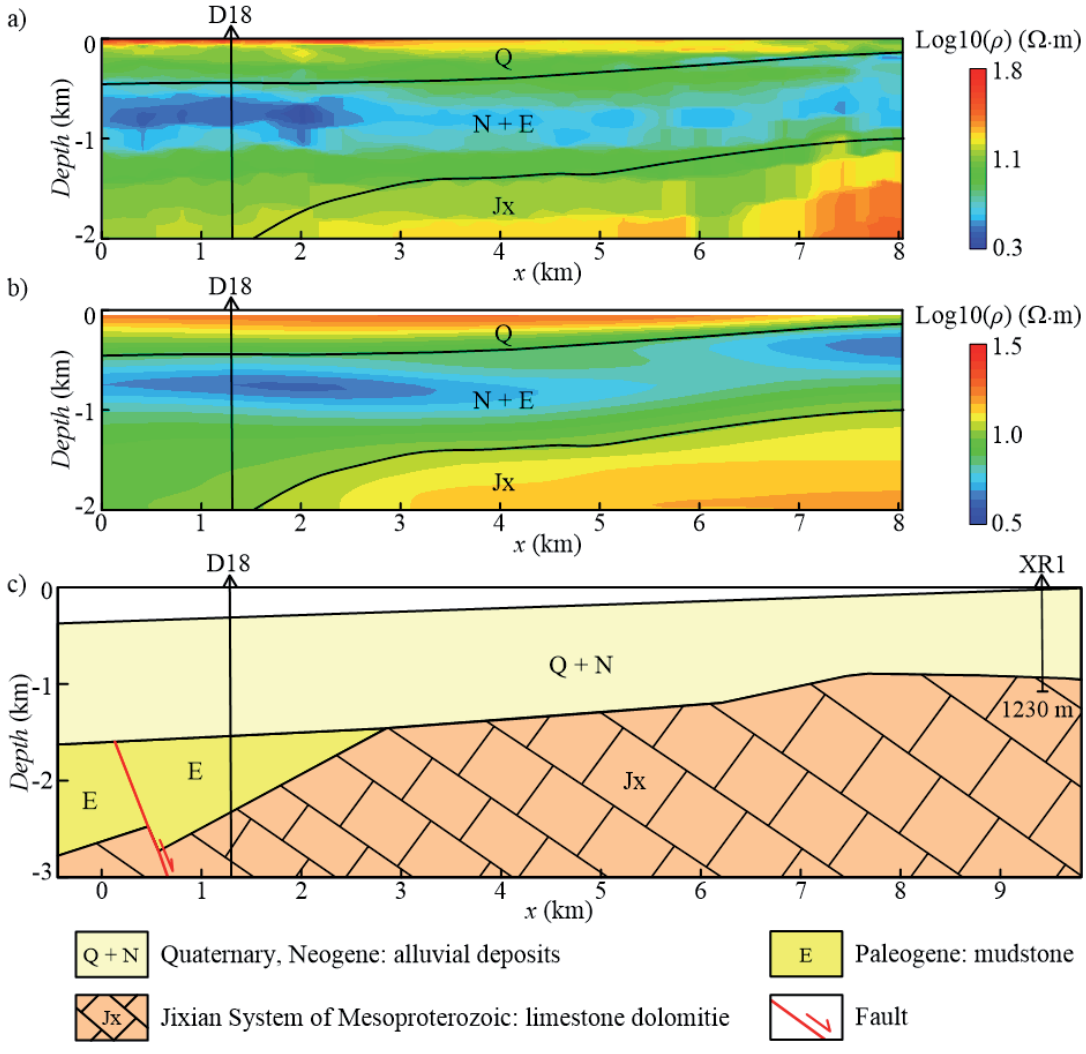

Fig. 13 - 1D (a) and 2D (b) inversion resistivity sections of the H_y full-field apparent resistivity; c) the geological profile (after Wang *et al.*, 2018)

7. Conclusions

1) The H_y component of CSAMT is not susceptible to static effects, nor is it shielded by a high-resistance shielding layer or restricted by bad grounding conditions, which can be used to detect ground resistivity. The H_y observation mode simplifies the working device. This approach can extend observational conditions to areas such as the Gobi Desert and permafrost and water areas.
2) Compared with the Cagniard and far-field apparent resistivity, there is no obvious distortion in the H_y full-field apparent resistivity, which can provide an initial inversion model. The tail branch of the H_y full-field apparent resistivity curve is closer to the true resistivity than those of E_x and H_z, which gives it certain advantages in reflecting deep electrical characteristics. In addition, the SNR of H_y is better than that of H_z under high noise levels.
3) Compared with the E_x full-field apparent resistivity, that of H_y is less affected by the angle φ. The H_y can be observed in the ranges of -30° to 30° (collinear zones) and 45°to 135° (broadside zones). Since the H_y full-field apparent resistivity is less affected by r than that of E_x, the signal level can be increased by reducing r.
4) Although the collinear H_y values are approximately half of the broadside H_y values, the former may be preferable because there is no need to address the double-solution phenomenon. For example, when the observation frequency range is narrow and the noise is high, the error in the transition zone may be large.

Acknowledgements. This research was sponsored by National Key R&D Program of China (2018YFC0603201) and Geological Survey Project of China (DD20189133).

REFERENCES

Asten M.W., Vicary M., Rutter H. and Cull J.P.; 2005: *An all-frequency resistivity-depth and static-correction technique for CSAMT data, with applications to mineralised targets under glacial cover (western Tasmania) and basalt cover (Victorian goldfields)*. Explor. Geophys., 36, 287-293.

Bai D. and Meju M.A.; 2003: *Deep structure of the Longling - Ruili fault underneath Ruili basin near the eastern Himalayan syntaxis: insights from magnetotelluric imaging*. Tectonophys., 364, 135-146.

Bartel L.C. and Jacobson R.D.; 1987: *Results of a controlled source audio-frequency magnetotelluric survey at the Puhimau thermal area, Kilauea Volcano, Hawaii*. Geophys., 52, 665-677.

Boerner D.E., Kurtz R.D. and Jones A.G.; 1993: *Orthogonality in CSAMT and MT measurements*. Geophys., 58, 924-934.

Chen W. and Xue G.; 2015: *The analysis and application of the vertical magnetic component in wide field electromagnetic method*. Geophys. Geochem. Explor., 39, 358-361, in Chinese.

Goldstein M.A. and Strangway D.W.; 1975: *Audio-frequency magnetotellurics with a grounded electric dipole source*. Geophys., 40, 669-683.

He J.S.; 2010: *Wide electromagnetic method and pseudo-random signal electric method*. Higher Education Press, Beijing, China, 214 pp., in Chinese.

Hou D., Xue G., Zhou N., He Y. and Chen W.; 2019: *Comparison between different apparent resistivity definitions of CSAMT*. J. Environ. Eng. Geophys., 24, 119-127.

Keller G.V.; 1988: *Rock and mineral properties.* In: Nabighian M.N. (ed), Electromagnetic methods in Applied Geophysics - Theory, vol. 1, Society of Exploration Geophysicists, Tulsa, OK, USA, pp. 13-52.

Lei D., Wu X., Di Q., Wang G., Lv X., Wang R., Yang J. and Yue M.; 2016: *Modeling and analysis of CSAMT field source effect and its characteristics*. J. Geophys. Eng., 13, 49-58.

Lei D., Di Q.Y., Wu J.J., Wang X.C., Liu Y.X., Fayemi O., Luan X.D. and Zhang W.W.; 2017: *Anti-interference test for the new SEP instrument: CSAMT study at Dongguashan Copper Mine, China*. J. Environ. Eng. Geophys., 22, 339-352.

Li D.Q.; 2017: *Measurement range of E-Ex and E-Eφ wide field electromagnetic methods*. Oil Geophys. Prospect., 52, 1315-1323.

Liu W.Q., Lin P.R., Lv Q.T., Li Y. and Li J.H.; 2018: *Synthetic modelling and analysis of CSEM full-field apparent resistivity response combining EM induction and IP effect for 1D medium*. Explor. Geophys., 49, 609-621.

Luan X.D., Di Q.Y. and Lei D.; 2018: *Near-field correction of CSAMT data based on Newton iteration method and GA method*. Chinese J. Geophys., 61, 4148-4159.

Maurer H.M.; 1988: *On: "Results of a controlled-source audio frequency magnetotelluric survey at the Puhimau thermal area, Kilauea Volcano, Hawaii," by Bartel L.C. and Jacobson R.D., authors (Geophys., 52, 665-677)*. Geophys., 53, 724-725, doi: 10.1190/1.1442507.

Routh P.S. and Oldenburg D.W.; 1999: *Inversion of controlled source audio-frequency magnetotellurics data for a horizontally layered earth*. Geophys., 64, 1689-1697.

Shlykov A.A. and Saraev A.K.; 2014: *Wave effects in the field of a high-frequency horizontal electric dipole.* Izv. Phys. Solid Earth, 50, 249-262.

Spies B.R. and Eggers D.E.; 1986: *The use and misuse of apparent resistivity in electromagnetic methods*. Geophys., 51, 1462-1471.

Sternberg B.K.; 1979: *Electrical resistivity structure of the crust in the southern extension of the Canadian shield - Layered earth models*. J. Geophys. Res.: Solid Earth, 84, 212-228.

Tang J.T. and He J.S.; 2005: *Methods and application of CSAMT method*. Central South University Press, Changsha, China, 336 pp., in Chinese.

Umesh C.D.; 1995: *Apparent resistivity curves in controlled-source electromagnetic sounding directly reflecting true resistivity in a layered earth*. Geophys., 60, 53-60.

Wang G.L., Li J., Wu A.M., Zhang W. and Hu Q.Y.; 2018: *A study of the thermal storage characteristics of Gaoyuzhuang Formation: a new layer system of thermal reservoir in Rongcheng uplift area, Hebei province*. Acta Geosci. Sin., 39, 24-32.

Wang J.L., Lin P.R., Wang M., Li D. and Li J.H.; 2017: *Three-dimensional tomography using high-power induced polarization with the similar central gradient array*. Appl. Geophys., 14, 291-300.

Wang J.L., Lin P.R., Wang M. and Li J.H.; 2019: *A multiple parameter extraction and electromagnetic coupling correction technique for time domain induced polarisation full waveform data*. Explor. Geophys, 50, 113-123.

Wang Q., Lin J., Yu S.B., Wang L.Q., Li B.B. and Zhu K.G.; 2015: *Calculation of sensitivities for airborne electromagnetic inversion progress*. J. Jilin Univ. (Eng. Tech. Ed.), 45, 2020-2025.

Wang X.J., He L.F., Chen L., Xu L.G., Lei X.Y. and Wei D.H.; 2016: *Maping deeply buried karst cavities using controlled-source audio magnetotellurics: a case history of a tunnel investigation in southwest China*. Geophys., 82, EN1-EN11.

Wilt M. and Stark M.; 1982: *A simple method for calculating apparent resistivity from electromagnetic sounding data*. Geophys., 47, 1100-1105.

Xue G.Q.; 2018: *The development of near-source electromagnetic methods in China*. J. Environ. Eng. Geophys., 23, 115-124.

Zhang Y.Y., Li X., Yao W.H., Zhi Q.Q. and Li J.; 2015: *Multi-component full field apparent resistivity definition of multi-source ground-airborne transient electromagnetic method with galvanic sources*. Chinese J. Geophys., 58, 2745-2758.

Zonge K.L. and Hughes L.J.; 1991: *Controlled source audio-frequency magnetotellurics.* In: Nabighian M.N. (ed), Electromagnetic methods in Applied Geophysics - Application, vol. 2, Society of Exploration Geophysicists, Tulsa, OK, USA, pp. 713-810, doi: 10.1190/1.9781560802686.ch9.

Corresponding author: Junlu Wang
School of Geophysics and Information Technology, China University of Geosciences
Beijing 10083, China
29 Xueyuan road, Beijing 10083, China
Phone: 86-13785465866; e-mail: wangjunlu2007@126.com